Journal of
Synchrotron
Radiation

ISSN 0909-0495

Received 29 July 2010
Accepted 24 September 2010

The study of the reconstructed three-dimensional structure of a solid-oxide fuel-cell cathode by X-ray nanotomography

Yong Guan,[a] Wenjie Li,[a] Yunhui Gong,[b] Gang Liu,[a] Jeff Gelb,[c] Xiaobo Zhang,[a] Ying Xiong,[a] Yangchao Tian[a]* and Haiqian Wang[b]*

[a]National Synchrotron Radiation Laboratory, University of Science and Technology of China, Hefei, Anhui 230029, The People's Republic of China, [b]Hefei National Laboratory for Physical Sciences at Microscale, University of Science and Technology of China, Hefei, Anhui 230026, The People's Republic of China, and [c]Xradia Inc., 5052 Commericial Circle, Concord, CA 94520, USA.
E-mail: ychtian@ustc.edu.cn, hqwang@ustc.edu.cn

The microstructure and morphology of solid-oxide fuel-cell electrodes are very complex but important because they strongly affect the electrical performance of the cell. In this work the high-resolution X-ray nanotomography technique is applied to reconstruct the three-dimensional microstructure of a $(La_{0.8}Sr_{0.2})_{0.95}MnO_3$ yttria-stabilized zirconia composite cathode. Some key microstructural parameters, such as the porosity, representative elementary volume, connected pore volume and pore phase tortuosity, were obtained based on the three-dimensional reconstruction volume data with a spatial resolution of sub-60 nm. These parameters bear intimate correlation with the efficiency of the electrochemical conversion process, and provide valuable information for optimizing the manufacturing processes and improving the device's reliability.

Keywords: X-ray nanotomography; solid-oxide fuel cell; phase tortuosity; pore connectivity.

1. Introduction

A solid-oxide fuel cell (SOFC) is an all-solid device that produces electricity directly from oxidizing a fuel and is a potential breakthrough technology for low-cost, clean and highly efficient production of electricity and heat. Redox reactions occur in the internal SOFC electrodes which are composed of porous materials; therefore, the microstructure of the electrode is likely to affect the electrochemical activity of a SOFC electrode. Advanced fuel-cell electrodes typically have complex internal microstructures that provide the necessary conditions for gas diffusion and electrochemical reaction. Thus, many groups have used various probing tools and methods to characterize the microstructures of SOFC electrodes (Ali *et al.*, 2008; Lanzini *et al.*, 2009; Allen *et al.*, 2009). However, these previous studies only revealed two-dimensional information about the electrode microstructure from sections or theoretically modelled the relationship between the performance of the SOFC and its electrode microstructure, and provided limited knowledge about the three-dimensional microstructure of the electrodes and how different regions are interconnected in a three-dimensional space. This calls for suitable three-dimensional microscopy methods to obtain three-dimensional information about SOFC electrodes for quantitative microstructural analysis. Indeed, three-dimensional reconstruction and analysis of SOFC electrodes has been performed previously using focused ion beam nanotomography (Gostovic *et al.*, 2007; Wilson & Barnett, 2008; Wilson, Duong *et al.*, 2009; Wilson, Gameiro *et al.*, 2009). This technique provided some very important parameters such as porosity, three-phase boundary length and tortuosity of specific phases, all of which were coupled with electrochemical simulation and used to study the performance of the SOFC anode, but came with limitations such as destruction of the internal structure.

A suitable tool for the non-destructive *in situ* characterization of three-dimensional microstructure of nanomaterials is X-ray computed nanotomography (nano-CT) (Chen, Wu *et al.*, 2008; Li *et al.*, 2009), which has also been applied to environmental science (Patty *et al.*, 2009) and bio-imaging (Le Gros *et al.*, 2005; Yang *et al.*, 2010; Chen *et al.*, 2010). The development of high-precision X-ray focusing optics has significantly improved the spatial resolution of X-ray microscopy. For instance, zone-plate-based soft X-ray microscopy with a spatial resolution of about 12 nm has been reported (Chao *et al.*, 2009). Full-field hard X-ray microscopy with Zernike phase contrast at 8 keV has reached a lateral resolution of better than 30 nm (Chen, Lo *et al.*, 2008). A SOFC sample with solid yttria-stabilized zirconia (YSZ) electrolyte and porous Ni–YSZ anode layers was imaged using laboratory-source-based X-ray computed tomography (Izzo *et al.*, 2008). Recently, this approach has been extended to

synchrotron radiation light sources. For example, full-field transmission X-ray microscopy has been applied to image directly a Ni–YSZ anode and the obtained results could be correlated well with the transport processes and losses within the pore and Ni–YSZ phase structures of a SOFC (Shearing *et al.*, 2010; Grew *et al.*, 2010).

In this paper, X-ray computed nanotomography based on a synchrotron radiation source has been used to image non-destructively the three-dimensional microstructure of a SOFC cathode material. The three-dimensional reconstruction data thus obtained allow us to calculate some critical parameters such as the porosity, pore space connectivity and tortuosity. All of these parameters may give useful hints to understanding the efficiency of the electrochemical conversion in the SOFC cathode.

2. Materials and methods

A bi-layered cathode was prepared from LSM [$(La_{0.8}Sr_{0.2})_{0.95}MnO_3$, Nextech, USA] and YSZ (TZ-8Y, Tosoh, Japan). The first LSM–YSZ (50:50 wt%) cathode functional layer (CFL) and the second LSM cathode current-collecting layer (CCCL) were screen-printed on top of the annealed sputtered YSZ film. Both layers were co-sintered at 1423 K for 3 h. In this study we chose the CFL as the sample.

2.1. X-ray microscope

The experiments were performed using the transmission hard X-ray microscope on beamline U7A at the National Synchrotron Radiation Laboratory, Hefei, China. The detailed experimental set-up of this X-ray microscope has been described elsewhere (Tian *et al.*, 2008). A 2.4 μm-thick Au phase plate was located at the back focal plane of the objective Fresnel zone plate to give negative Zernike phase-contrast enhancement at 8 keV. This nano-CT system achieves a spatial resolution down to 60 nm.

An appropriate piece of sample was glued to the end of the tungsten scanning tunneling microscope tip fixed on the sample holder, and then 181 two-dimensional projections were collected at angles ranging from −90° to +90° in 1° intervals. After background subtraction and alignment, tomographic data were subsequently reconstructed by using Xradia software (Tkachuk *et al.*, 2007). Using the tomographic data, a series of cross-section slices were generated without actual sectioning and saved into binary data format for further data analysis.

3. Results and discussion

Zernike phase-contrast imaging mode was used at 8 keV to image the CFL. One of the two-dimensional cross-section slices is shown in Fig. 1(*a*), where the white portion denotes solid material and black is the pore space. First, the reconstructed volume data are converted from greyscale to binary format in order to calculate the porosity. Then, based on the best threshold method (Chow & Kaneko, 1972), an image segmentation iterative algorithm has been developed and used to identify the appropriate threshold value of the volume data. The maximum and the minimum grey values of the binary image were calculated and named T_{max} and T_{min}, respectively. The initial threshold T_0 was set as $(T_{max} + T_{min})/2$. Based on T_0 the image was segmented into two parts. The mean value of one part was calculated and named T_{1m}, and that of the other part was T_{2m}. Then a new threshold $T_2 = (T_{1m} + T_{2m})/2$ was obtained. This iteration continued until $T_k = T_{k+1}$, which was the eventual threshold value. If the grey value of a binary voxel is equal or less than the threshold, the voxel is set to the pore phase; otherwise it is set to the solid material. Fig. 1(*b*) shows the segmented image, which is the same slice as shown in Fig. 1(*a*). Then the cubic three-dimensional transparent rendering (see Fig. 2*b*) was reconstructed based on the segmented volume. The side length of the cubic three-dimensional transparent rendering is 6.0 μm, corresponding to 103 pixels, meaning that the calibrated cube size of one pixel is 58.3 × 58.3 × 58.3 nm in the nano-CT system. The porosity, calculated by dividing the sum of the number of voxels assigned to the pore phase by the total number of voxels, turned out to be about 39.0%. This microstructural parameter is critical for understanding the electrochemical properties of SOFC cathodes owing to its effects on oxygen transport in the electrode.

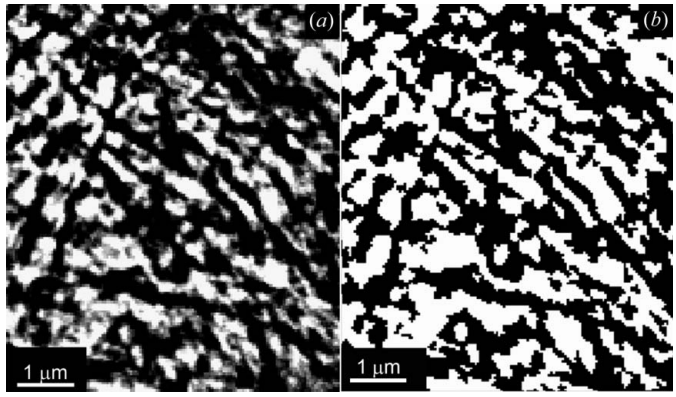

Figure 1
(*a*) One-pixel-thick reconstruction slice of CFL, where the material is white and pore space is black, and (*b*) the segmented slice after thresholding.

Below a certain volume size the porosity of the reconstructed volume is not representative of the entire CFL owing to local structure effects. Thus it is necessary to ensure whether the porosity of the reconstructed volume can represent the entire volume of the CFL. To this end, the 'expansion method' was developed to determine the representative volume size. A sketch map of this method is shown in Fig. 2(*a*). One vertex of the reconstructed volume was selected arbitrarily as a starting point, then a number of sub-volumes that used the starting point as their common vertex were obtained by increasing the side length of the cube in the *x*, *y* and *z* directions. Simultaneously, the porosity of each cubic volume was calculated. In this study three vertices of the reconstructed volume were chosen as the starting points. Fig. 2(*b*) shows the relationship between sub-volume size and its porosity.

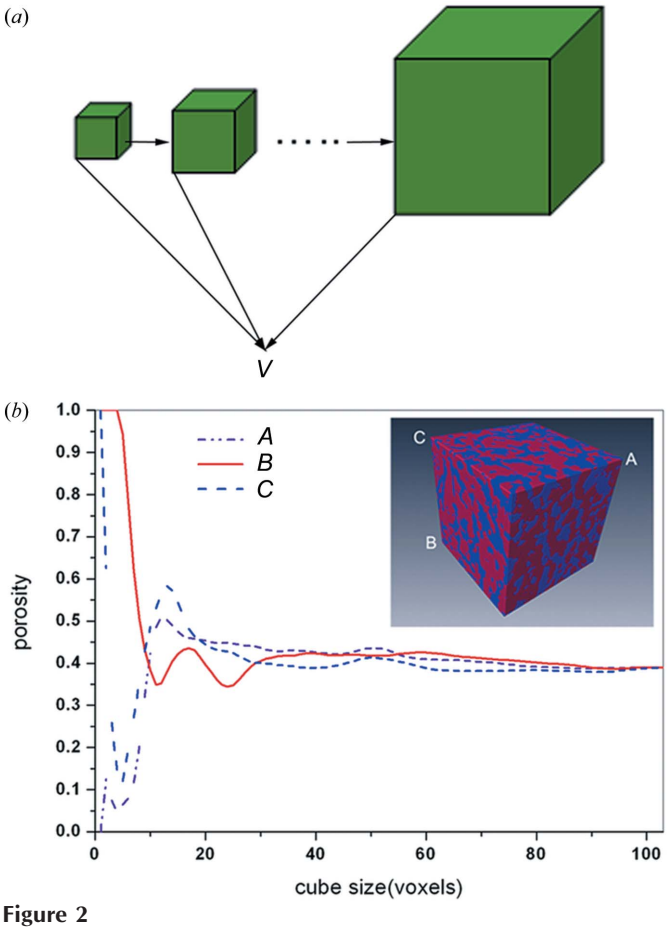

Figure 2
(*a*) Sketch map of the expansion method, where the point *V* is the chosen vertex. (*b*) Chart of the measured porosity as a function of cube size. From this figure the minimum representative volume was determined to be ∼70 voxels per side (∼4.1 µm).

Evidently, the calculated porosity fluctuates with increasing sub-volume size. However, the calculated porosity converges to a certain value when the side of the sub-volume reaches 4.1 µm (equivalent to 70 pixels per side), suggesting a macroscopic homogeneity. Thus, the reconstructed volume of size 6 × 6 × 6 µm can be extended to represent the entire CFL in this study.

Another important parameter affecting the efficiency of the gas conduction (pore) phase is the pore connectivity. The segmented volume data were also used to calculate the percentages of connected pore and unconnected pore phases based on a method that we developed which is similar to the 'burning' method (Bentz & Garboczi, 1991). To illustrate the connectivity, a two-dimensional sketch map is shown in Fig. 3, where the black region represents the pore phase. In this map the connected, dead end and isolated pores were defined. According to this definition, the connectivity of the pore space was calculated in the full three-dimensional volume. First, one side of the image was defined as the input end and the other one as the output end. Pore voxels in the input end were chosen as the start points using the algorithm. Any pore voxel that touched these start points was set to the same value. From the input to the output end, the voxels that had the same value

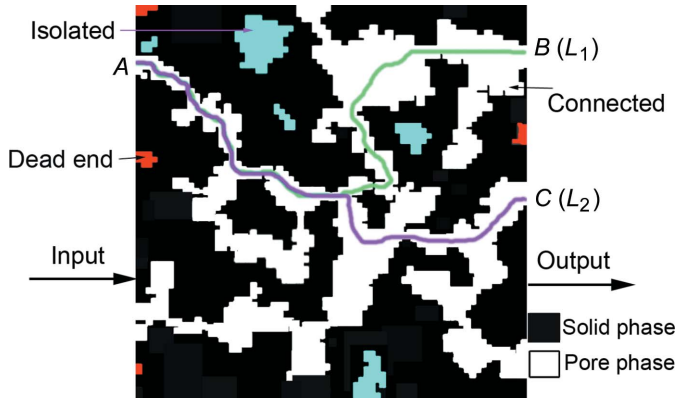

Figure 3
Conceptual representation of the connectivity of the pore phase and its tortuosity. Pore phase is shown in white and solid phase is shown in black. Isolated pores, connected regions and dead end pores are indicated. Point *A* is the starting point, *B* and *C* are two end points corresponding to *A*. L_1 and L_2 are the effective path lengths.

were considered to form a spanning cluster. Analogously, from the output to the input end, another spanning cluster was obtained. By comparing these two spanning clusters, the regions where they did not overlap were considered to be dead ends. The overlapped regions between these two spanning clusters were identified as connected regions. Then, the number of connected pores and dead end pores were calculated. The sum of voxels that represent the isolated regions were also obtained by subtracting the total number of connected and dead end pores from the total voxels of three-dimensional volume. Finally, the connected porosity and disconnected porosity were calculated by dividing the number of their respective voxels by the total pore volume.

Fig. 4(*a*) shows a three-dimensional rendering structure illustrating the solid phases (red), connected pore phases (blue) and unconnected pore phases (green). Further analysis reveals that the connected porosity of the CFL is 38.6%, which occupies 98.9% of the whole pore space. The unconnected porosity is 0.4%, which corresponds to unconnected pore space (including the isolated volume and dead pores). Shown in Fig. 4(*b*) is the spatial distribution of the unconnected pore space, which is almost isolated in the three-dimensional microstructure of the CFL and, thus, cannot make contributions to gas transport. We note that the X-ray nanotomography technique can also be applied to other SOFC electrode materials and can help to improve their performance *via* optimizing their microstructure for gas transport.

Finally, we discuss the tortuosity of a pore phase which is defined as the ratio of the path length of a pore to the material thickness and can affect the performance of the SOFC (Wilson *et al.*, 2006). Pore-phase tortuosity was measured using a method that we developed and is described briefly below. A conceptual representation of the tortuosity is shown in Fig. 3. In the input end, one pore pixel (*A*, see Fig. 3) was selected as the starting point. The pore pixels that contacted the starting point were given the same value. Finally, the point *A* would reach the output side by diffusion and there are many terminal points, such as *B* and *C*. Then the lengths of the effective path

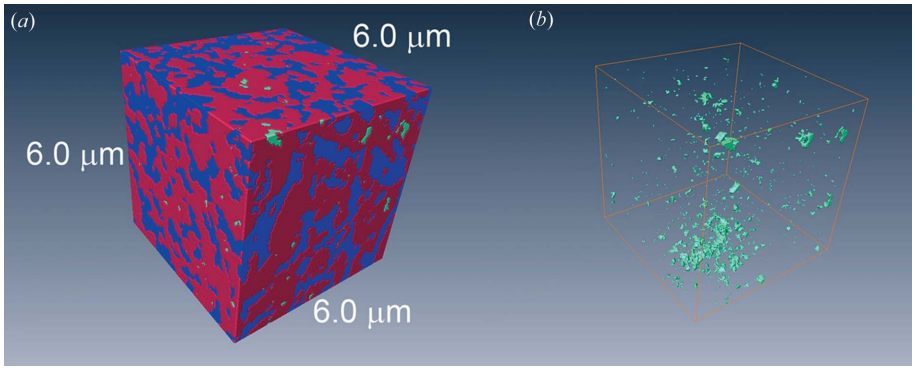

Figure 4
(*a*) A three-dimensional cathode rendering, labelling the solid (red), connected pore (blue) and unconnected pore phases (green). (*b*) A three-dimensional distribution of unconnected pore space (blue).

(L_1 and L_2 in Fig. 3) between the starting point and the terminal points were calculated. Similar concepts and methods were extended to the full three-dimensional morphology. The tortuosity of the pore phase was obtained using the average of all these calculated effective path lengths divided by the distance between the input end and output. The tortuosity values in the x, y and z directions were found to be 1.32, 1.28 and 1.30, respectively. They all are close to the value of 1.5 reported previously (Steele, 2000).

4. Conclusion

In this study the three-dimensional microstructure of a CFL was successfully reconstructed using X-ray computed tomography. This technique is demonstrated to be a useful tool for quantifying porous cathode microstructures. It opens up the possibility of understanding the quantitative relationship between electrode microstructure and performance, and may find extensive applications in analyzing, optimizing and designing other multiphase material systems in the future.

This work was supported by grants from the 985 Project of the State Ministry of Education, the National Natural Science Foundation of China (10675113, 10734070) and the Knowledge Innovation Program of the Chinese Academy of Sciences (KJXC2-YW-N43).

References

Ali, A., Wen, X., Nandakumar, K., Luo, B. J. & Chuang, K. T. (2008). *J. Power Sources*, **185**, 961–966.
Allen, A. J., Ilavsky, J. & Braun, A. (2009). *Adv. Eng. Mater.* **11**, 495–501.
Bentz, D. P. & Garboczi, E. J. (1991). *Cement Concrete Res.* **21**, 325–344.
Chow, C. K. & Kaneko, T. (1972). *Comput. Biomed. Res.* **5**, 388–410.
Chao, W., Kim, J., Rekawa, S., Fischer, P. & Anderson, E. H. (2009). *Opt. Express*, **17**, 17669–17677.
Chen, J., Wu, C. Y., Tian, J. P., Li, W. J., Yu, S. H. & Tian, Y. C. (2008). *Appl. Phys. Lett.* **92**, 233104.
Chen, J., Yang, Y., Zhang, X., Andrews, J. C., Pianetta, P., Guan, Y., Liu, G., Xiong, Y., Wu, Z. & Tian, Y. (2010). *Anal. Bioanal. Chem.* **397**, 2117–2121.
Chen, Y. T., Lo, T. N., Chu, Y. S., Yi, J., Liu, C. J., Wang, J. Y., Wang, C. L., Chiu, C. W., Hua, T. E., Hwu, Y., Shen, Q., Yin, G. C., Liang, K. S., Lin, H. M., Je, J. H. & Margaritondo, G. (2008). *Nanotechnology*, **19**, 395302.
Gostovic, D., Smith, J. R., Kundinger, D. P., Jones, K. S. & Wachsman, E. D. (2007). *Electrochem. Solid State Lett.* **10**, B214–B217.
Grew, K. N., Chu, Y. S., Yi, J., Peracchio, A. A., Izzo, J. R., Hwu, Y., De Carlo, F. & Chiu, W. K. S. (2010). *J. Electrochem. Soc.* **157**, B783–B792.
Izzo, J. R., Joshi, A. S., Grew, K. N., Chiu, W. K. S., Tkachuk, A., Wang, S. H. & Yun, W. B. (2008). *J. Electrochem. Soc.* **155**, B504–B508.
Lanzini, A., Leone, P. & Asinari, P. (2009). *J. Power Sources*, **194**, 408–422.
Le Gros, M. A., McDermott, G. & Larabell, C. A. (2005). *Curr. Opin. Struc. Biol.* **15**, 593–600.
Li, W. J., Wang, N., Chen, J., Liu, G., Pan, Z. Y., Guan, Y., Yang, Y. H., Wu, W. Q., Tian, J. P., Wei, S. Q., Wu, Z. Y., Tian, Y. C. & Guo, L. (2009). *Appl. Phys. Lett.* **95**, 053108.
Patty, C., Barnett, B., Mooney, B., Kahn, A., Levy, S., Liu, Y. J., Pianetta, P. & Andrews, J. C. (2009). *Environ. Sci. Technol.* **43**, 7397–7402.
Shearing, P. R., Gelb, J. & Brandon, N. P. (2010). *J. Eur. Ceram. Soc.* **30**, 1809–1814.
Steele, B. C. H. (2000). *Solid State Ion.* **134**, 3–20.
Tian, Y. C., Li, W. J., Chen, J., Liu, L. H., Liu, G., Tkachuk, A., Tian, J. P., Xiong, Y., Gelb, J., Hsu, G. & Yun, W. B. (2008). *Rev. Sci. Instrum.* **79**, 103708.
Tkachuk, A., Duewer, F., Cui, H. T., Feser, M., Wang, S. & Yun, W. B. (2007). *Z. Kristallogr.* **222**, 650–655.
Wilson, J. R. & Barnett, S. A. (2008). *Electrochem. Solid State Lett.* **11**, B181–B185.
Wilson, J. R., Duong, A. T., Gameiro, M., Chen, H. Y., Thornton, K., Mumm, D. R. & Barnett, S. A. (2009). *Electrochem. Commun.* **11**, 1052–1056.
Wilson, J. R., Gameiro, M., Mischaikow, K., Kalies, W., Voorhees, P. W. & Barnett, S. A. (2009). *Microsc. Microanal.* **15**, 71–77.
Wilson, J. R., Kobsiriphat, W., Mendoza, R., Chen, H. Y., Hiller, J. M., Miller, D. J., Thornton, K., Voorhees, P. W., Adler, S. B. & Barnett, S. A. (2006). *Nat. Mater.* **5**, 541–544.
Yang, Y. H., Li, W, J., Liu, G., Zhang, X. B., Chen, J., Wu, W. Q., Guan, Y., Xiong, Y., Tian, Y. & Wu, Z. (2010). *J. Microsc.* **240**, 14–20.